In-plane antiferromagnetic moments in axion topological insulator candidate $EuIn_2As_2$

Yang Zhang,[1,*] Ke Deng,[2,*] Xiao Zhang,[1] Meng Wang,[1] Yuan Wang,[2] Cai Liu,[2] Jia-Wei Mei,[2] Shiv Kumar,[3] Eike F. Schwier,[3] Kenya Shimada,[3] Chaoyu Chen,[2,†] and Bing Shen[1,‡]

[1] *School of Physics, Sun Yat-Sen University, Guangzhou, Guangdong 510275, China*
[2] *Shenzhen Institute for Quantum Science and Engineering (SIQSE) and Department of Physics, Southern University of Science and Technology, Shenzhen 518055, China*
[3] *Hiroshima Synchrotron Radiation Center, Hiroshima University, Higashihiroshima, Hiroshima 739-0046, Japan*

(Dated: February 26, 2022)

Topological insulator with antiferromagnetic order can serve as an ideal platform for the realization of axion electrodynamics. In this paper, we report a systematic study of the axion topological insulator candidate $EuIn_2As_2$. A linear energy dispersion across the Fermi level confirms the existence of the proposed hole-type Fermi pocket. Spin-flop transitions occur with magnetic fields applied within the *ab*-plane while are absent for fields parallel to the *c*-axis. Anisotropic magnetic phase diagrams are observed and the orientation of the ground magnetic moment is found to be within the *ab*-plane. The magnetoresistivity for $EuIn_2As_2$ behaves non-monotonic as a function of field strength. It exhibits angular dependent evolving due to field-driven and temperature-driven magnetic states. These results indicate that the magnetic states of $EuIn_2As_2$ strongly affect the transport properties as well as the topological nature.

I. INTRODUCTION

Axion topological insulator (ATI) is an exotic material which can host hypothetic quasiparticles axions within the Standard Model of particle physics[1,2]. Axion electrodynamics emerge on the surface of topological insulators with magnetic order. It can be described by the formula

$$S_\theta = \frac{\theta e^2}{4\pi^2}\int dt d^3\mathbf{x}\mathbf{E}\cdot\mathbf{B} \quad (1)$$

where $\mathbf{E}$ and $\mathbf{B}$ are electromagnetic fields and the axion angle $\theta{=}\pi$ gives rise to topological magnetoelectric (TME) effect[1,3]. The ATI is realizable in various artificial structures such as sandwich heterostructures but still unreachable in the intrinsic materials up to now[4,5]. Recently theoretical calculations predicted that axion topological states were able to exist in the intrinsic materials with antiferromagnetic (AF) order spontaneously breaking the time-reversal symmetry (TRS)[6–11].

The van der Waals (vdW) Mn-Bi-Te family of materials were proposed magnetic topological insulators with the intrinsic *A*-type AF order, which could host quantum anomalous Hall effect (QAHE) with a non-zero Chern number[11]. Recent neutron experiments observed this *A*-type magnetic order in $MnBi_2Te_4$ agreeable with the prediction of ATI[12]. And in the ultra thin flakes or films of $MnBi_2Te_4$, a moderate magnetic field could drive the system into a Chern insulating state exhibiting zero longitudinal resistance and quantized Hall resistance h/e^2 (QAHE) as well as favoring the former prediction[13–15]. Nonetheless, subsequent Angle-resolved Photoelectron Spectroscopy (ARPES) results indicated that the Dirac surface states were gapless crossing the projected bulk band gap[16–24]. Moreover, the neutron scattering experiments revealed that the short range magnetic order existed in a wide temperature region companying with strong magnetic fluctuation in $MnBi_2Te_4$[25]. These results indicate that the magnetic surface configuration and the topological states in $MnBi_2Te_4$ should be treated carefully.

Different from layered vdW $MnBi_2Te_4$, $EuIn_2As_2$ exhibits a three-dimensional structure and crystallizes in the $P6(3)/mmc$ space group (in Fig. 1(a))[27]. It is an AF topological insulator candidate[22,34] with tunable high-order topological insulating states (HOTIS) and axion topological insulating states (ATIS)[10]. Particularly, the non-trivial topological states are strongly influenced by the detailed magnetization according to the theoretical calculations[10]. Although the ground state AF order is along the *c*-axis for $EuIn_2As_2$, manipulating the direction of magnetic moments allows for archiving different topological states: in-plane magnetic moments result in an ATIS with gapped surface states while the out-of-plane magnetic moments lead to a HOTIS with hinge state on the domain wall of two gapped surfaces[10]. The investigation of the detailed magnetization for $EuIn_2As_2$ is needed and necessary to gain the insight of its topological nature. In this paper, we systemically study $EuIn_2As_2$ by combining magneto-transport measurements and angle-resolved photoemission spectroscopy measurements . A spin-flop transition is observed by applying small magnetic fields within the *ab*-plane. Anisotropic magnetic phase diagrams reveal in-plane AF moment agreeable with the ATI prediction. The field and temperature driven magnetic states dominate the transport properties in low temperature region. The observed hole-type Fermi surface made up of a linear dispersing band indicates that pristine $EuIn_2As_2$ is a metal instead of insulator. Further tuning chemical potential such as doping or gating the system may realize ATIS in this intrinsic material.

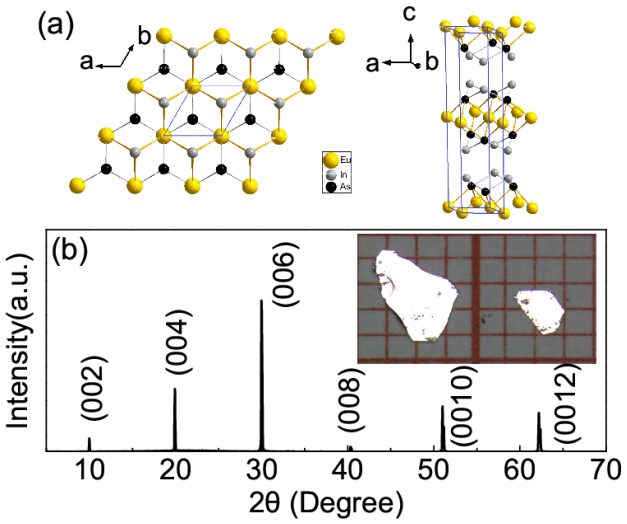

Figure 1. (a) Crystal structure of $EuIn_2As_2$. (b) X-ray diffraction pattern of a single crystaline $EuIn_2As_2$. High crystallinity is indicated by the set of (00l) peaks. Inset: picture of typical single crystals of $EuIn_2As_2$.

II. EXPERIMENTAL DETAIL

$EuIn_2As_2$ single crystals were grown via the self-flux method. Eu, In, and As were mixed stoichiometrically and sealed inside an evacuated quartz tube. The mixture was heated to 1000 ^{o}C, slowly cooled to 700 ^{o}C, and finally decanted by a centrifuge. Planar single crystals with the dimensions of 2×3×0.3 mm^3 were harvested as shown in the inset of Fig.1 (b). Geometric structure and elemental composition were confirmed by X-ray diffraction (XRD) and Wavelength-dispersive spectroscopy (WDS). Sharp peaks in the XRD confirm high crystalline quality of the samples (Fig. 1 (b)).

Detailed structural information was summarized in Table 1. Rietveld refinements were carried out with the SHELXL software. ARPES measurements were performed at Beamline 1 of Hiroshima Synchrotron Radiation Center (HSRC), Hiroshima University, Japan, with a VG Scienta R4000 electron analyzer[26]. The photon energy was fixed at 30 eV. The beam was linearly polarized with its polarization lying in the measurement and incidence plane. The energy and angular resolutions were set at 25 meV and 0.2^o, respectively. Samples were cleaved at 30 K and measured at 20 K, both at vacuum better than 2×10^{-11} mbar. For the magneto transport measurements rectangular samples were selected to fabricate into devices to avoid influence of geometry on the results (Fig.2 (a)). Electronic contacts were added via patterned mask with photolithography subsequent growth of Ti/Au(10nm/100nm) layers. Electrical transport measurements were performed in Quantum design Physical Properties Measurement System (QD PPMS Dynacool). Direct current (DC) magnetization and alternating current (AC) susceptibility measurements were performed in Quantum Design Magnetic Property Measuring System (MPMS).

Table I. The crystal data and structure refinement for $EuIn_2As_2$ at 150 K.

Empirical formula	$EuIn_2As_2$
Formula weight	531.44
Crystal system	hexagonal
Space group	P63/mmc
unit cell dimensions	a=4.2068(5)Å
	b=4.2068(5)Å
	c=17.849(3)Å
α	90^o
β	90^o
γ	120^o
Volume	273.55(8) Å^3
Z	2
ρ(calc)	6.452 g/cm^3
μ	31.511 mm^{-1}
F(000)	454.0
Radiation	MoK α (λ= 0.71073)
2θ range for data collection	9.136^o to 69.908^o
Index ranges	$6 \leq h \leq 6$,
	$-5 \leq k \leq 3$,
	$-20 \leq l \leq 28$
Independent reflections	271 [R_{int} = 0.0462,
	R_σ = 0.0443]
Data/restraints/parameters	271/0/10
Goodness-of-fit on F^2	1.023
Final R indexes [I $\geq 2\sigma$ (I)]	R_1 = 0.0315,
	ωR_2 = 0.0741
Final R indexes [all data]	R_1 = 0.0434,
	ωR_2 = 0.0784
Largest diff. peak/hole / e Å^3	1.63/-1.87

III. RESULTS AND DISCUSSION

Figure 2 shows the temperature dependent resistivity $\rho(T)$ and magnetization of $EuIn_2As_2$. The system behaves metallic in the high temperature region (shown in Fig.1 (a)) and exhibits a peak in $\rho(T)$ at 18 K indicative of an AF transition reported previously[27]. The temperature dependent DC magnetization $M(T)$ and AC susceptibility $\chi'(T)$ shown in Fig. 2 (b) are consistent with this transition to an AF ground state. Above the AF transition temperature T_N, an obvious broad peak of the imaginary part of the AC susceptibility χ'' is observed around 40 K. The related non-zero response of χ'' persists up to the temperatures far above T_N due to Eu^{2+} spin dynamics. The $M(T)$ curve as well as starts to deviate from Curie Weiss behavior below 150 K (also far above T_N) which is linked with the deviation from a

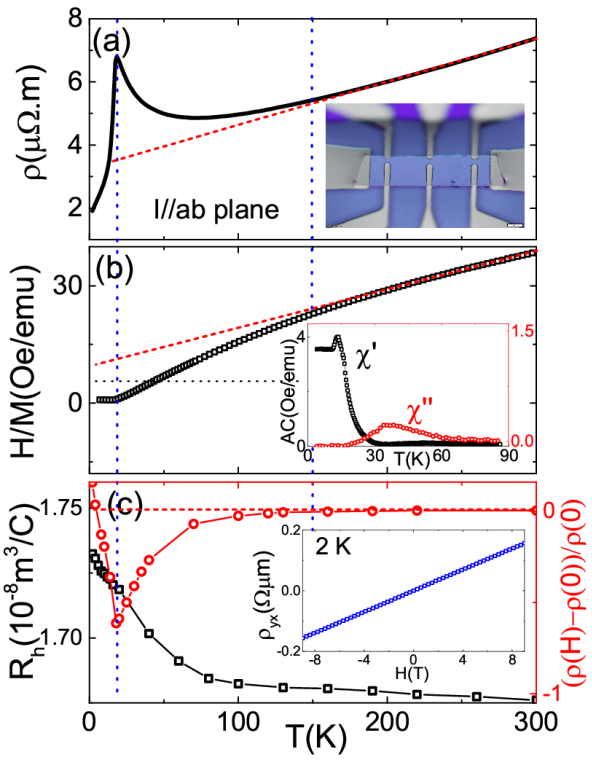

Figure 2. (a) Temperature dependent resistivity of $EuIn_2As_2$ within the *ab*-plane. Above 150 K the curve is quasi linear. The red dashed line is used to estimate the deviation from the linear behaviour below 150 K. Inset: Picture of $EuIn_2As_2$ with patterned contacts used for the measurement. (b) Temperature dependent DC magnetization of $EuIn_2As_2$ with magnetic field of $H = 1$ T applied within the *ab*-plane. Deviation from the Curie-Weiss behaviour (marked by the red dashed line) is observed below 150 K. Inset: Temperature dependent AC susceptibility measured with an amplitude of 1 Oe and a frequency of 1000 Hz. The imaginary part χ'' is zero below 18 K and exhibits a broad peak around 35 K. (c) Temperature dependence of MR at 1 T with $H//c$ is plotted in red. Hall coefficient is plotted in black, respectively. Obvious MR is observed below 150 K and a transition from negative to positive MR occurs around 18 K. The inset: Field dependent Hall resistivity ρ_{xy} at 2 K exhibits a linear behavior.

quasi-linear temperature dependence $\rho(T)$ shown in Fig. 1 (a). These results indicate that the strong short-range AF fluctuation state may exist in a wide temperature region extending well above T_N inconsistent instead of the paramagnetic state. Such a scenario would explain the observed anisotropic *g*-shift and a line width broadening above T_N revealed by Electron spin resonance (ESR) measurements[28]. Further weight is given to the proposed SR-AF phase by the temperature dependent magnetoresistivity (MR) measurements in Fig. 2 (c). The MR (defined as MR=$\rho(H)/\rho(0\ \mathrm{T})$-1) above 150 K is negligible consisted with the paramagnetic state while it becomes obvious below 150 K and reach to the largest negative value at T_N. Below T_N the negative MR is suppressed when $EuIn_2As_2$ enters the AF ground state. It changes the sign to positive at 4 K and reaches up to the largest positive value of 30% at 2 K. This behavior was observed in antiferromagnets crossing the metamagnetic phase transition due to appearance of various local magnetic moments[29]. The positive Hall coefficient shown in Fig. 2 (d) exhibits an slight upturn of less than 3% towards lower temperatures. This small upturn may be resulted from local spin alignment changing the carrier effective mass or carrier concentration. Both carrier density and effective mass can be determined by measurements of the temperature dependence of the electronic band structure by Angle-Resolved Photoelectron Spectroscopy (ARPES). However, the variation of less than 3% is difficult to resolve in our ARPES measurements and out of the focus of the current work.

Figure 3 shows ARPES spectra of the electronic structure of $EuIn_2As_2$ measured at 20 K. Three valence bands α, β, γ (from low to high binding energy) near Fermi level were observed along the K-G-K high symmetry direction of the surface Brillouin zone (Fig. 3(a)). The fully occupied β and γ band originate from bulk states, while the only band crossing the Fermi level (α) is surface derived[22]. Fig. 3(b) shows the constant energy contours of the band structure, with one at and the other one 500 meV below the Fermi level. A circular hole-like pocket formed by α grows in sizes with increasing binding energy agrees well with Fig. 3(a). A zoom in of Fig. 3(a) enables us to scrutinize the dispersion of the surface band and fit the energy dispersion $\mathbf{E}(\mathbf{k})$ using MDC cuts. The extracted $\mathbf{E}(\mathbf{k})$ curve is linear with Fermi velocity of 3.7 eV·A (5.7105 m/s) and k_F =0.12 1/Å.(Fig. 3(c,d)). In addition, we note that by using the extracted k_F and Fermi velocity, the Dirac point can be estimated as 300 meV above Fermi level. Further tuning the chemical potential by doping or gating electron would lift the Fermi level close to the Dirac point.

Theoretical calculations proposed two distinct AF ground states with different orientation of the magnetic moment but the small energy difference for $EuIn_2As_2$. The detailed investigation of the magnetic phase diagram is therefore vital to understand or even control the proposed non trivial topological states in this material. To this end, both DC magnetic susceptibility and magnetotransport measurements were performed in single crystals of $EuIn_2As_2$ with magnetic fields applied within the *ab*-plane ($H//ab$) and along the *c*-axis ($H//c$) respectively. The field dependent magnetization $M(H)$ curves at 2 K are shown in Fig. 4(a) exhibiting anisotropic behavior. Increasing the applied magnetic field along *ab*-plane to a critical value H_{sp}, a small jump accompanying a magnetic hysteresis in $M(H)$ is observed, which indicates a first order magnetic transition (shown in the inset of Fig. 4(a)). This abnormal behaviour is more clearly identified by a sharp peak in the $\mathrm{d}M/\mathrm{d}H$ curves shown in Fig. 4(b). The magnetization saturates when further increasing the magnetic field to the critical value H_{sa}. As with $H//c$, no additional magnetic transition occurs

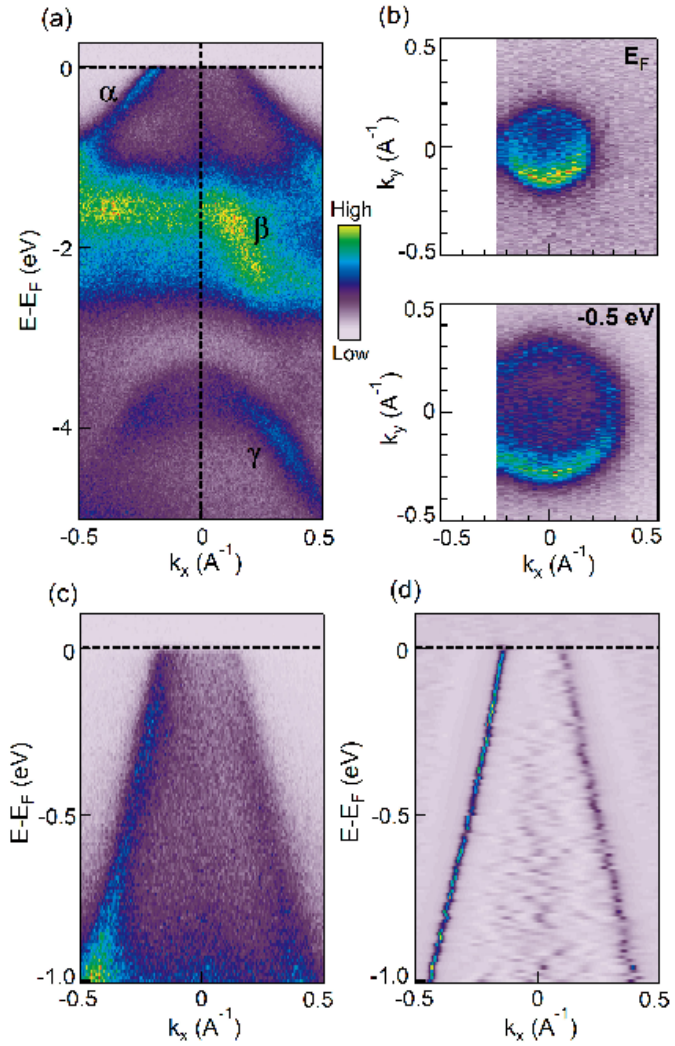

Figure 3. (a) Valence band structure along the K-G-K high symmetry direction. Valence bands are labeled from low toward higher binding energy as α, β, and γ. The α state is surface derived as discussed in previous work[22]. (b) Fermi surface map (top) and constant energy contour at 0.5 eV below the Fermi level. (c) Zoom-in of the surface state close to the Fermi level. (d) The corresponding MDC second derivative of (c) to highlight its linear dispersion.

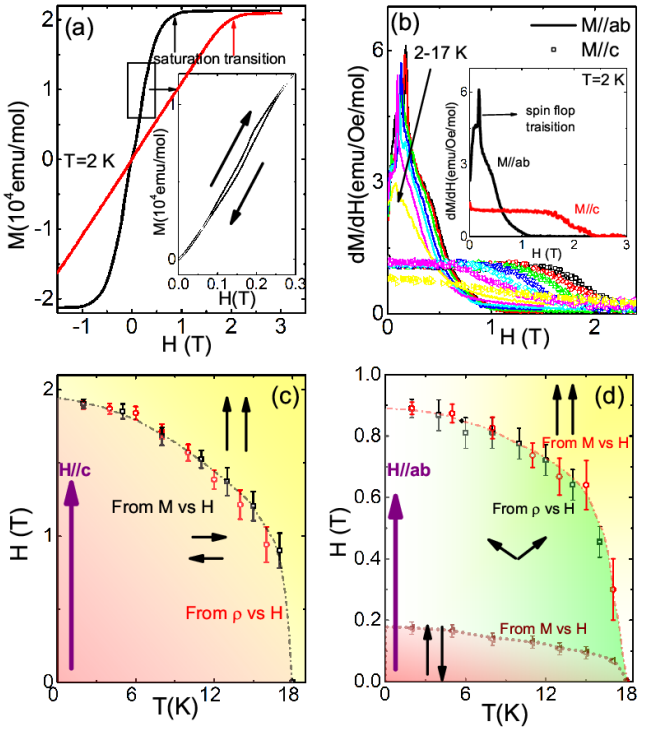

Figure 4. (a) Magnetic hysteresis loops (MH) for $EuIn_2As_2$ with $H//ab$ (black lines) and $H//c$ (red line) at 2 K. The MH curves in the region marked with a rectangle is zoomed and shown in the inset. A jump of the hysteresis is observed in the MH curves, if field is applied within the ab-plane. (b) Derivative of MH ($\mathrm{d}M/\mathrm{d}H$) at 2 K, 5 K, 8 K, 11 K, 13 K, 15 K, and 17 K with applied field within the ab-plane (marked with lines) and c-axis (marked with open symbols), respectively. Inset: $\mathrm{d}M/\mathrm{d}H(H)$ at 2 K with $H//ab$ (marked with black line) and $H//c$ (marked with red line). We can observe a sharp peak related to spin flop transition with $H//ab$. (c) and (d) The phase diagram of $EuIn_2As_2$ with $H//ab$ and $H//c$, respectively. The purple arrow indicates the direction of applied magnetic field. The black arrows indicate the direction of Eu^{2+} spins

besides the saturation (occurred at $H_{sa}^{\perp}$) shown in Fig. 4(a) and (b). Such anisotropic magnetic behavior can be interpreted within the picture of spin-flop transitions: in a collinear AF system, increasing the applied field to a critical value H_{sp} along, or nearly parallel to its magnetic easy axis (MEA), the AF sub-lattice magnetizations M_1 and M_2 rotate abruptly[30]. The staggered magnetization $L = M_1 - M_2$ directs perpendicular to the original MEA instead of aligning itself with the external field direction since the system energy is lower in the former case. This so called spin-flop transition is usually a first-order phase transition and can be detected by a jump in the magnetization loop or a peak in field dependent heat capacity.[30,31]. Further increasing the applied magnetic field above H_{sp} will gradually tilt the spin-flopped moments towards the direction of the external magnetic field and finally align all the spins' moments well along at H_{sp}. Thus, two transitions will be observed in the case of applied filed parallelled to MEA. On the other hand, with the applied field perpendicular to the MEA, the AF sublattice spins tilt gradually and finally were well aligned by external field directly at a critical field $H_{sa}^{\perp}$. As shown in Fig. 5(c) and (d), applying the magnetic field along different directions gives rise to the anisotropic magnetic phases diagram of $EuIn_2As_2$.

In a simple localized collinear AF system, the magnetization is mainly determined by AF exchange interaction, magnetocrystalline anisotropic energy and Zeeman energy. Considering the single ion case the Hamiltonian

can be written as

$$H = -J\sum \vec{S}_i \cdot \vec{S}_j - D\sum S_{iz}^2 + D\sum S_{jz}^2 - g\mu_B H_0(\sum S_{iz} + \sum S_{jz}) \quad (2)$$

where S_i and S_j are the spins at site i and j of the sublattice, H_0 is the applied static magnetic field along the z direction, J is the exchange constant of the interaction between spins S_i and S_j[32]. The D-term represents the uniaxial anisotropy of a the single ion and the last term is the usual Zeeman term. With the field applied parallel to the MEA, the molecular field approximation based on a semiclassical model gives critical fields at T=0 K as:

$$H_{sp}(0) = (H_A(2H_E - H_A))^{0.5} \quad (3)$$

$$H_{sa}(0) = 2H_E - H_A \quad (4)$$

and with fields applied perpendicular to the MEA, only the single critical field $H_{sa}^{\perp}(0)$ exists and can be expressed as:

$$H_{sa}^{\perp}(0) = 2H_E + H_A \quad (5)$$

where the H_E=$zJ/g\mu_B$ is the exchange field, H_A= $D/g\mu_B$ is the anisotropy field, and z is the number of nearest neighbors. By extrapolating the experimental $H_{sp}(T)$, $H_{sa}(T)$, and $H_{sa}^{\perp}(T)$ curves to 0 K in Fig 4.(c) and (d), the $H_{sp}(0)$ and $H_{sa}(0)$ and $H_{sa}^{\perp}(0)$ are estimated to be 0.18 T, 1.05 T, and 2.1 T respectively. Employing formulas (2) and (4), we calculate that H_A=0.03 T and H_E= 0.54 T. According to formula (3), the calculated $H_{sp}(0)$=0.7 T is much larger than the experimental value of 0.19 T. It is reminiscent of the overestimated values in nickel oxide which was attributed to the existence of abnormal spin wave modes[33]. The presence of magnetic fluctuation above T_N as discussed above, together with the mismatch of experimental and theoretical H_{sp} give weight to the hypothesis that $EuIn_2As_2$ is in a state of fluctuating spin-waves. Such a non-standard spin wave excitation can not be understood by semiclassical picture and would explain the deviation of the extracted critical fields. Inelastic neutron scattering experiments are needed and necessary to probe the spin excitation in $EuIn_2As_2$.

In a magnetic system, the detailed magnetization could strongly affect the transport properties of a material such as the $EuSn_2As_2$[34,35]. As shown in Fig. 5 (a) the MR for $EuIn_2As_2$ exhibits a monotone evolution with both $H//ab$ and H//c closely relating to the detailed magnet states. Below T_N (18 K), the observed positive MR in the low field region increases with rising applied field to the maximum value around the saturation fields H_{sa} and $H_{sa}^{\perp}$. Further increasing the magnetic field, the MR decreases and eventually become negative at higher fields. The peak in field dependent magnetoresitivity MR(H)

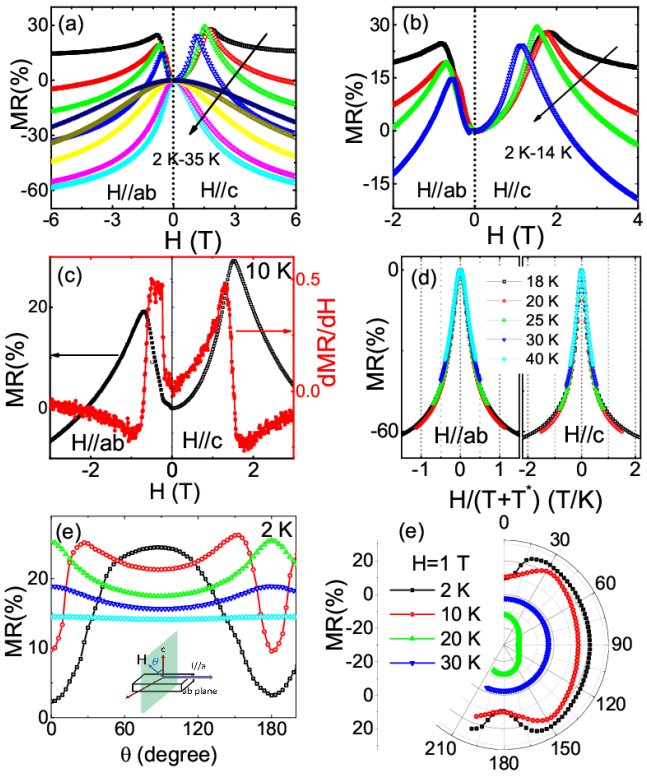

Figure 5. (a) MR for $EuIn_2As_2$ at 2 K, 6 K, 10 K,14 K, 16 K, 18 K, 20 K, and 30 K with $H//ab$ and $H//c$ respectively. (b) Zoomed MR for $EuIn_2As_2$ at 2 K, 6 K, 10 K,14 K with $H//ab$ and $H//c$ respectively. (c) Zoomed MR and dM/dH at 10 K with $H//ab$ and $H//c$ respectively. (d) Scaled MR at 18 K, 20 K, 25 K, 30 K and 35 K with $H//ab$ and $H//c$ respectively. (e) The AMR at 2 K with H=0.5 T, 1 T, 2 T, 3 T, and 6 T. Inset: Schematic configuration of the rotating sample. (f) Angular dependence of MR at 2 K , 10 K, 20 K, and 30 K with H=1 T

curve moves towards lower fields as well as reduces the intensity with increasing the temperature and finally disappears at T_N. Such a feature is characteristic of a metamagnetic phase transition[36] agreeable with our magnetization results (see Fig. 4). The difference of MR for $H//ab$ and $H//c$ is mainly due to the appearance of spin-flop states with $H//ab$ below T_N shown in Fig. 5 (b). The kinked MR(H)curves are observed for $H//ab$ near the spin-flop region while the MR varies smoothly with H for $H//c$ below the saturation fields. The kink in $M(H)$ caused by the appearance of spin-flopped magnetic domains is more clear in the dMR/dH at 10 K shown in Fig. 5 (c). The various magnetic states mainly contribute to the anisotropic magneto-transport properties below T_N. Above T_N, the MR curves behave Kondo-like. In a Kondo-type AF system, the spin scattering by localized magnetic moments will be suppressed by aligning local moments giving rise to a negative MR[27]. By using the Bethe-Ansatz method[36], the MR(H) curves at vari-

ous temperatures can be scaled on to a single curve with the relation:

$$\mathrm{MR}(H) = f(\frac{H}{T+T^*}) \quad (6)$$

as shown in Fig. 5 (d). For $H//ab$ and $H//c$, the characteristic temperature T^* is acquired to be -14.1 K and -14 K respectively. The negative value indicates the presence of ferromagnetic correlations within the AF ground-state of $EuIn_2As_2$[36].

The angular dependent magnetoresistivity (AMR) is shown in Fig. 5 (e) and (f) with the measurement configuration shown in the inset of Fig. 5 (e). The current flows within the *ab*-plane and the magnetic field is applied and rotates within a plane perpendicular to the current. Magnetic field-induced changes in the AMR symmetry are observed. At 2 K , a two-fold symmetric MR is observed with a maximum value in the direction of $H//ab$ (H=0.5 T). Increasing the applied field, MR exhibits a maximum for the direction of $H//$c (H=2 T) due to the canted spins. Further increasing the field, the MR becomes isotropic as shown in Fig.5.(e). With increasing the temperature, the angular MR exhibits a similar symmetry evolving with H=1 T and changes the value from positive to negative shown in Fig.5(g). Magnetic field-induced changes in the AMR have also been observed in other topological materials such as $ZrTe_5$ and $EuTiO_3$[37,38]. The applied magnetic field controls both the spin canting as well as Zeeman splitting leading to topological phase transitions such as the movement of Weyl points[37,38]. For an AF topological insulator, the detailed magnetization of such a system are key to the topological nature and controllable by various ways. As shown in this paper, $EuIn_2As_2$ exhibits various magnetic states tunable by temperature, magnetic field strength and direction suggesting the possibility of various topological states and transitions in this material.

IV. CONCLUSION

The electronic structure and transport properties are systemically studied for the ATI candidate $EuIn_2As_2$. Hole-type Fermi pockets are revealed and their linear energy dispersion near Fermi level agrees with the proposed topological state around the Γ-point. External magnetic fields applied within the *ab*-plane lead to spin-flop transitions suggesting in-plane AF magnetic moments of the ground state. The anisotropic magnetic phase diagrams are revealed and the temperature and field driven magnetic states lead to the systemic evolving of the transport properties in the low temperature region. These results reveal the detailed magnetization of $EuIn_2As_2$ and its potential to realize tunable axion states or other non trivial topological states.

Work at SYSU were supported by the Hundreds of Talents program of Sun Yat-Sen University, the Fundamental Research Funds for the Central Universities, NSFC-11904414, NSF of Guangdong under Contract No.2018A030313055, and Physical Research Platform (PRP) in School of Physics, SYSU. The ARPES experiments at HiSOR were performed with the approval of it Proposal Assessing Committee (Proposal Numbers 19AG004).

* The authors contribute to equal
† Corresponding author: chency@sustech.edu.cn
‡ Corresponding author: shenbingdy@mail.sysu.edu

[1] X.-L. Qi, T. L. Hughes, and S.-C. Zhang, Phys. Rev. B **78**, 195424 (2008).
[2] R. Li, J. Wang, X. L. Qi, and S. C. Zhang, Nat. Phys. **6**, 284 (2010).
[3] F. Wilczek, Phys. Rev. Lett. **58**, 1799 (1987).
[4] M. Mogi, M. Kawamura, R. Yoshimi, A. Tsukazaki, Y. Kozuka, N. Shirakawa, K. S. Takahashi, M. Kawasaki, and Y. Tokura, Nat. Mater. **16**, 516 (2017).
[5] Di Xiao, Jue Jiang, Jae-Ho Shin, Wenbo Wang, Fei Wang, Yi-Fan Zhao, Chaoxing Liu, Weida Wu, Moses H.W. Chan, Nitin Samarth, and Cui-Zu Chang, Phys. Rev. Lett. **120**, 056801 (2018).
[6] Dongqin Zhang, Minji Shi, Tongshuai Zhu, Dingyu Xing, Haijun Zhang, Jing Wang, Phys. Rev. Lett. **122**, 206401 (2019).
[7] Sugata Chowdhury, Kevin F. Garrity, and Francesca Tavazza, npj Computational Materials **5**, 33 (2019).
[8] Alexander Zeugner, Frederik Nietschke, Anja U. B. WolterSebastian, GaRaphael C. Vidal, Thiago R. F. PeixotoDarius, PohlChristine Damm, Axel Lubk, Richard Hentrich, Simon K. Moser, Celso Fornari, Chul Hee Min, Sonja Schatz, Katharina Kiner, Maximilian Unzelmann, Martin Kaiser, Francesco Scaravaggi, Bernd Rellinghaus, Kornelius Nielsch, Christian Hess, Bernd BÃŒchner, Friedrich Reinert, Hendrik Bentmann, Oliver Oeckler, Thomas Doert, Michael Ruck, Anna Isaeva, Chem. Mater. **31** 82795 (2109).
[9] M. M. Otrokov, I. P. Rusinov, M. Blanco-Rey, M. Hoffmann, A. Yu. Vyazovskaya, S. V. Eremeev, A. Ernst, P. M. Echenique, A. Arnau, and E. V. Chulkov, Phys. Rev. Lett. **122**, 107202 (2019).
[10] Yuanfeng Xu, Zhida Song, Zhijun Wang, Hongming Weng, and Xi Dai, Phys. Rev. Lett. **122**, 256402 (2019).
[11] Jiaheng Li, Yang Li, Shiqiao Du, Zun Wang, Bing-Lin Gu, Shou-Cheng Zhang, Ke He, Wenhui Duan, Yong Xu, Science Advances **14**, 5685 (2019).
[12] J.-Q. Yan, Q. Zhang, T. Heitmann, Zengle Huang, K. Y. Chen, J.-G. Cheng, Weida Wu, D. Vaknin, B. C. Sales, and R. J. McQueeney, Phys. Rev. Materials **3**, 064202 (2019).
[13] Yujun Deng, Yijun Yu, Meng Zhu Shi, Jing Wang, Xian Hui Chen, Yuanbo Zhang, arXiv:1904.11468 (2019).
[14] Jun Ge, Yanzhao Liu, Jiaheng Li, Hao Li, Tianchuang Luo, Yang Wu, Yong Xu, Jian Wang, arXiv:1907.09947 (2019).
[15] Chang Liu, Yongchao Wang, Hao Li, Yang Wu, Yaoxin Li, Jiaheng Li, Ke He, Yong Xu, Jinsong Zhang, Yayu Wang,

arXiv:1905.00715 (2019).

[16] R. C. Vidal, H. Bentmann, T. R. F. Peixoto, A. Zeugner, S. Moser, C. H. Min, S. Schatz, K. Kissner, M. Unzelmann, C. I. Fornari, H. B. Vasili, M. Valvidares, K. Sakamoto, J. Fujii, I. Vobornik, T. K. Kim, R. J. Koch, C. Jozwiak, A. Bostwick, J. D. Denlinger, E. Rotenberg, J. Buck, M. Hoesch, F. Diekmann, S. Rohlf, M. Kallane, K. Rossnagel, M. M. Otrokov, E. V. Chulkov, M. Ruck, A. Isaeva, F. Reinert, arXiv:1903.11826 (2019).

[17] Bo Chen, Fucong Fei, Dongqin Zhang, Bo Zhang, Wanling Liu, Shuai Zhang, Pengdong Wang, Boyuan Wei, Yong Zhang, Zewen Zuo, Jingwen Guo, Qianqian Liu, Zilu Wang, Xuchuan Wu, Junyu Zong, Xuedong Xie, Wang Chen, Zhe Sun, Dawei Shen, Shancai Wang, Yi Zhang, Minhao Zhang, Xuefeng Wang, Fengqi Song, Haijun Zhang, Baigeng Wang, arXiv:1903.09934 (2019).

[18] Yan Gong, Jingwen Guo, Jiaheng Li, Kejing Zhu, Menghan Liao, Xiaozhi Liu, Qinghua Zhang, Lin Gu, Lin Tang, Xiao Feng, Ding Zhang, Wei Li, Canli Song, Lili Wang, Pu Yu, Xi Chen, Yayu Wang, Hong Yao, Wenhui Duan, Yong Xu, Shou-Cheng Zhang, Xucun Ma, Qi-Kun Xue, Ke He, Chin. Phys. Lett. **36**, 076801 (2019).

[19] Hao Li, Shengsheng Liu, Chang Liu, Jingsong Zhang, Yong Xu, Rong Yu, Yang Wu, Yuegang Zhang, Shoushan Fan, arXiv:1907.13018 (2019).

[20] Y. J. Chen, L. X. Xu, J. H. Li, Y. W. Li, C. F. Zhang, H. Li, Y. Wu, A. J. Liang, C. Chen, S. W. Jung, C. Cacho, H. Y. Wang, Y. H. Mao, S. Liu, M. X. Wang, Y. F. Guo, Y. Xu, Z. K. Liu, L. X. Yang, Y. L. Chen, arXiv:1907.05119 (2019)

[21] Przemyslaw Swatek, Yun Wu, Lin-Lin Wang, Kyungchan Lee, Benjamin Schrunk, Jiaqiang Yan, Adam Kaminski, arXiv:1907.09596 (2019).

[22] Hang Li, Shunye Gao, Shaofeng Duan, Yuanfeng Xu, Kejia Zhu, Shangjie Tian,Wenhui Shan,Zhicheng Rao,Jierui Huang, Jiajun Li, Zheng-Tai Liu, Wan-Ling Liu, Yao-Bo Huang, Yu-Liang Li, Yi Liu, Guo-Bin Zhang, He-Chang Lei, You-Guo Shi, Wen-Tao Zhang, Hong-Ming Weng, Tian Qian, Hong Ding, arXiv:1907.06491 (2019).

[23] Yu-Jie Hao, Pengfei Liu, Yue Feng, Xiao-Ming Ma, Eike F. Schwier, Masashi Arita, Shiv Kumar, Chaowei Hu, Rui'e Lu, Meng Zeng, Yuan Wang, Zhanyang Hao, Hongyi Sun, Ke Zhang, Jiawei Mei, Ni Ni, Liusuo Wu, Kenya Shimada, Chaoyu Chen, Qihang Liu, Chang Liu, arXiv:1907.03722 (2019).

[24] Chaowei Hu, Xiaoqing Zhou, Pengfei Liu, Jinyu Liu, Peipei Hao, Eve Emmanouilidou, Hongyi Sun, Yuntian Liu, Harlan Brawer, Arthur P. Ramirez, Huibo Cao, Qihang Liu, Dan Dessau, Ni Ni, arXiv:1905.02154 (2019).

[25] J. -Q. Yan, D. Pajerowski, Liqin Ke, A. M. Nedic, Y. Sizyuk, Elijah Gordon, P. P. Orth, D. Vaknin, R. J. McQueeney, arXiv:1908.02332 (2019).

[26] H. Iwasawa, K. Shimada, E. F. Schwier, M. Zheng, Y. Kojima, H. Hayashi, J. Jiang, M. Higashiguchi, Y. Aiura, H. Namatame and M. Taniguchi, J. Synchrotron Rad. **24**, 836 (2017).

[27] Andrea M. Goforth, Peter Klavins, James C. Fettinger, and Susan M. Kauzlarich, Inorg. Chem. **47**, 11048 (2019).

[28] P. F. S. Rosa, C. Adriano, T. M. Garitezi, R. A. Ribeiro, Z. Fisk, and P. G. Pagliuso, Phys. Rev. B **86**, 094408 (2012).

[29] A. P. Pikul, D. Kaczorowski, T. Plackowski, and A. Czopnik, H. Michor, E. Bauer, G. Hilscher, P. Rogl and Yu. Grin. Phys. Rev. B **67**, 224417 (2003).

[30] Y. Shapira and S. Foner, Phys. Rev. B **1**, 3083 (1970).

[31] Hai-Feng Li, npj Computational Materials **2**, 16032 (2016).

[32] C. C. Becerra, N. F. Oliveira, Jr., A. Paduan-Filho, W. Figueiredo, and M. V. P. Souza, Phys. Rev. B **38**, 6887 (1988).

[33] F. L. A. Machado, P. R. T. Ribeiro, J. Holanda, R. L. Rodriguez-Suarez, A. Azevedo, and S. M. Rezende, Phys. Rev. B **95**, 104418 (2017).

[34] Xin Gui, Ivo Pletikosic, Huibo Cao, Hung-Ju Tien, Xitong Xu, Ruidan Zhong, Guangqiang Wang, Tay-Rong Chang, Shuang Jia, Tonica Valla, Weiwei Xie, Robert J. Cava, arXiv:1903.03888 (2019).

[35] Hang Li, Shun-Ye Gao, Shao-Feng Duan, Yuan-Feng Xu, Ke-Jia Zhu, Shang-Jie Tian, Wen-Hui Fan, Zhi-Cheng Rao, Jie-Rui Huang, Jia-Jun Li, Zheng-Tai Liu, Wan-Ling Liu, Yao-Bo Huang, Yu-Liang Li, Yi Liu, Guo-Bin Zhang, He-Chang Lei, You-Guo Shi, Wen-Tao Zhang, Hong-Ming Weng, Tian Qian, Hong Ding, arXiv:1907.06491 (2019).

[36] P. Schlottmann, Phys. Rep. **181**, 1 (1989).

[37] G. Zheng, X. Zhu, Y. Liu, J. Lu, W. Ning, H. Zhang, W. Gao, Y. Han, J. Yang, H. Du, K. Yang, Y. Zhang, and M. Tian, Phys. Rev. B **96**, 121401(R) (2017).

[38] Kaveh Ahadi, Xuezeng Lu, Salva Salmani-Rezaie, Patrick B. Marshall, James M. Rondinelli, and Susanne Stemmer, Phys. Rev. B **99**, 041106(R) (2019).